Functionalized Graphene for High-Performance Two-Dimensional Spintronics Devices

Linze Li,[†] Rui Qin,[†] Hong Li, Lili Yu, Qihang Liu, Guangfu Luo, Zhengxiang Gao, and Jing Lu*

State Key Laboratory of Mesoscopic Physics and Department of Physics, Peking University, Beijing 100871, People's Republic of China. [†] These authors contributed equally to this work.

ABSTRACT Using first-principles calculations, we explore the possibility of functionalized graphene as a high-performance two-dimensional spintronics device. Graphene functionalized with O on one side and H on the other side in the chair conformation is found to be a ferromagnetic metal with a spin-filter efficiency up to 54% at finite bias. The ground state of graphene semifunctionalized with F in the chair conformation is an antiferromagnetic semiconductor, and we construct a spin-valve device from it by introducing a magnetic field to stabilize its metallic ferromagnetic state. The resulting room-temperature magnetoresistance is up to 2200%, which is 1 order of magnitude larger than the available experimental values.

KEYWORDS: functionalized graphene · spintronics · spin-filter efficiency · magnetoresistance · first-principles calculations

Graphene has a long spin relaxation time and length[1−6] due to a small spin−orbit coupling of carbon atoms, and this makes graphene a promising material in applications of spintronics. Spin-valve and spin-filter are two kinds of popular spintronics devices. Graphene-based spin-valves have been experimentally constructed, but the resulting magnetoresistance (MR) is quite small. A 10% MR is observed in a spin-valve with a graphene wire contacted by two soft magnetic electrodes at 300 K.[7] A spin-valve consisting of a graphene flake and ferromagnetic electrodes shows a 12% MR at 7 K when a MgO tunnel barrier is inserted at the graphene/electrode interface.[8] Unlike graphene, which is a nonmagnetic zero-bandgap semiconductor, zigzag graphene nanoribbons (ZGNRs) have a magnetic moment on the two edges. A high-performance spin-valve with giant magnetoresistance (GMR) can be constructed by either using a ferromagnetic ZGNR connected to two ferromagnetic electrodes[9,10] (first type) or using an antiferromagnetic ZGNR connected to two metal electrodes[11] (second type). The first type of device functions *via* changing the relative direction of the local magnetic field applied on the electrodes, and the second type of device does so by applying a magnetic field on the antiferromagnetic ZGNR. ZGNRs are also predicted to be a half-metal when a transverse electrical field is applied,[12] the two edges are differently functionalized,[13] or they are rolled into nanoscrolls.[14] However, at present, graphene nanoribbons with nanometer scale width cannot be produced with desirable experimental control, and production of dense arrays of ordered graphene nanoribbons remains a big challenge.[15,16] One fundamental question arises: Is it possible to fabricate high-performance spin-valves and spin-filters from two-dimensional graphene instead of one-dimensional ZGNRs?

Functionalization of graphene is a possible scheme to attain such a goal. Fully hydrogenated graphene, which is referred to as "graphane", was predicted theoretically[17] and later synthesized through two different chemical approaches.[18,19] Graphane is a nonmagnetic semiconductor with a direct bandgap of 3.43 eV.[20] Graphene functionalized by groups beyond the hydrogen such as graphene oxide[21] and graphene fluoride[22−24] have also been synthesized. Recent experiments demonstrated that fully covered graphene fluoride samples exhibit strong insulating behavior,[24] which is in agreement with a large bandgap of ∼3.5 eV.[25] One type of one-side fluorine-functionalized graphene has also been realized, and the F coverage saturates at 25% (C_4F).[23] This provides additional freedom of functionalization of graphene. Interestingly, a computational work using density functional theory (DFT) predicted that single-side hydrogenated graphene (C_2H), which is referred to as "graphone", is a ferromagnetic semiconductor with an indirect bandgap of 0.46 eV.[26] The cause lies in that half-hydrogenation makes the electrons in the unhydrogenated carbon atoms localized and unpaired and

* Address correspondence to jinglu@pku.edu.cn.

Received for review September 22, 2010 and accepted March 11, 2011.

Published online March 11, 2011
10.1021/nn102492g

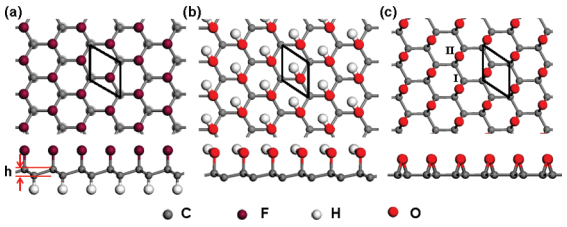

Figure 1. Top and side views of the chair conformation of the (a) F-graphene-H, (b) OH-graphene, and (c) O-graphene. The rhombus marked in black shows the primitive cells. I and II represent two different bond types.

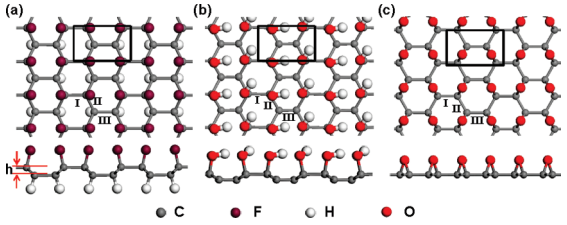

Figure 2. Top and side views of the boat conformation of the (a) F-graphene-H, (b) OH-graphene, and (c) O-graphene. The rectangle marked in black shows primitive cells. I, II, and III represent three different bond types.

the magnetic moments at these sites couple ferromagnetically. By synthetically incorporating molecular building blocks, graphane-like and porous-graphene-like polymers have been obtained experiemntally.[27,28] Notably, Kim *et al*. proposed one novel organic graphene-like polymer, 2,4,6-tri(1,3,5-triazinyl)methyl radical polymer, which is predicted to be half-metallic in terms of the DFT calculations.[29]

The existence of magnetism in single-side hydrogenated graphene suggests possible application of functionalized graphene as highly effective spintronics materials. In this article, using the DFT and nonequilibrium Green's function (NEGF) method, we explore the possibility of fabricating high-performance spintronics devices from functionalized graphenes. We consider two types of functionalization schemes. One is functionalization on one side of graphene (the number of functional groups equals half the number of C atoms), and the other is different functionalizations on the two sides of graphene (the number of each kind of functional groups equals half the number of C atoms). Both boat and chair conformations have been considered. A highly polarized metallic ferromagnet is obtained when graphene is functionalized with O on one side and H on the other side in the chair conformation, and GMR is obtained in a spin-valve based on graphene functionalized by F on one side in the chair conformation. New avenues are therefore opened for application of graphene in high-performance two-dimensional spintronics devices.

RESULTS AND DISCUSSION

We consider five different functionalized graphenes: graphene functionalized with F (F-graphene), O (O-graphene), or OH (OH-graphene) on only one side and graphene functionalized with H on one side and with F (F-graphene-H) or O (O-graphene-H) on the other side. As each functionalized graphene has both chair and boat conformations, we calculate 10 different structures in total.

We begin our study by optimizing the geometric structures of the 10 different functionalized graphenes in their nonmagnetic state. The difference in geometry between different magnetic states is negligibly small. We present the chair and boat conformations of some functionalized graphenes in Figure 1 and Figure 2, respectively. All the chair conformations have rhombic primitive cells (marked in black in Figure 1) containing two C atoms, and all the boat conformations have rectangular primitive cells (marked in black in Figure 2) containing four C atoms. In all the structures except the O-graphene, C atoms of the graphene layer are corrugated, forming two atom sublayers, and the F and O atoms are above one C atom. We display the optimized structure of the chairlike and boatlike F-graphene-H in Figure 1a and Figure 2a, respectively. The structure of the chairlike O-graphene-H is similar to that of the chairlike F-graphene-H, and each O atom still has an unpaired electron after functionalization. In the boatlike O-graphene-H, two O atoms sitting above two nearest C atoms form a single bond with a length of 1.50 Å. In the OH-graphene (Figure 1b and 2b), all the H atoms tend to sit above the center of the hexagonal ring of graphene. As shown in Figures 1c and 2c, the O atoms of the O-graphene sit above the carbon−carbon bonds and form two bonds with two carbon atoms ([2+1] cycloaddition), leaving all the C atoms in one layer. Here we define the fully functionalized graphene as graphene in which all the C atoms in the graphene layer are functionalized, such as O-graphene, F-graphene-H, O-graphene-H, and graphane. Correspondingly, in the semifunctionalized graphene, such as

TABLE 1. Structural Parameters of the Optimized Functionalized Graphenes: Lattice Parameters (*a*, *b*, γ), Length of the C−C Bond inside the Graphene (d_{C-C}), Distance between the Functional Group and Its Nearest C Atom (d_{FG-C}), Thickness of the Corrugation of Graphene (*h*), and Angle (θ) of ∠C−O−C and ∠C−O−H in the O-Graphene and OH-Graphene, Respectively[a]

chair conformation	F-graphene	OH-graphene	graphone	O-graphene	F-graphene-H	O-graphene-H	graphane
a (Å)	5.09	5.13	5.05	5.24	5.14	5.07	5.07
b (Å)	5.09	5.13	5.05	5.32	5.14	5.07	5.07
γ (deg)	120.0	120.0	120.0	119.5	120.0	120.0	120.0
d_{C-C} (Å)	1.50	1.51	1.50	1.54 (I) 1.51 (II)	1.56	1.56	1.53
d_{FG-C} (Å)	1.49	1.51	1.15	1.43	1.39 (F−C) 1.11 (C−H)	1.36 (O−C) 1.11 (C−H)	1.11
h (Å)	0.30	0.35	0.32	0	0.47	0.54	0.46
θ		∠C−O−H: 105.6°		∠C−O−C: 63.6°			
boat conformation	**F-graphene**	**OH-graphene**	**graphone**	**O-graphene**	**F-graphene-H**	**O-graphene-H**	**graphane**
a (Å)	5.12	5.13	4.97	5.28	5.10	5.07	4.99
b (Å)	5.14	5.20	5.08	5.38	5.16	5.15	5.05
γ (deg)	120.2	119.8	120.7	119.4	119.6	120.5	120.3
d_{C-C} (Å)	1.63 (I) 1.53 (II) 1.36 (III)	1.68 (I) 1.54 (II) 1.38 (III)	1.55 (I) 1.50 (II) 1.35 (III)	1.58 (I) 1.52 (II) 1.53 (III)	1.63 (I) 1.55 (II) 1.60 (III)	1.54 (I) 1.55 (II) 1.56 (III)	1.57 (I) 1.54 (II)
d_{FG-C} (Å)	1.42	1.51	1.13	1.42	1.38 (F−C) 1.10 (C−H)	1.45 (O−C) 1.11 (C−H)	1.10
h (Å)	0.41	0.43	0.40	0	0.63	0.59	0.65
θ		∠C−O−H: 106.3°		∠C−O−C: 64.3°			

[a] Each supercell contains eight C atoms. Structural parameters of the 2D hexagonal lattice supercell of pristine graphene that contains eight C atoms are $a = b = 4.92$ Å and $\gamma = 120°$.

F-graphene, OH-graphene, and graphone, only half the C atoms in graphene layer are functionalized. In the fully functionalized graphene, all the sp^2-hybridized C atoms become sp^3-hybridized upon functionalization. In the semifunctionalized graphene, only half the C atoms that are functionalized become sp^3-hybridized.

The geometric parameters of all the checked functionalized graphenes and graphone and graphane are displayed in Table 1. All the supercells are enlarged upon functionalization. The magnitudes of lattice enlargement mainly depend on the type of functional groups. O atoms cause the largest lattice increase with a magnitude of about 8%, while H atoms cause the smallest one, with a magnitude of about 3%. After functionalization, all the chair conformations have only one type of C−C bond except the chairlike O-graphene, which has two types (I and II in Figure 1c), while all the boat conformations have three different types of C−C bonds (I, II, and III in Figure 2). Therefore, in all the boatlike structures and the chairlike O-graphene, the symmetry of the hexagonal lattice is broken by functionalization. The C−C bond lengths (from 1.50 to 1.63 Å, typical of a C−C single bond) of both the fully functionalized and semifunctionalized graphenes in the chair conformation and the fully functionalized graphene in the boat configuration are significantly larger than that of the pristine graphene (1.42 Å). In the semifunctionalized boat conformation, the lengths of type III bonds range from 1.35 to 1.38 Å, indicative of formation of C═C double bonds between two unfunctionalized C atoms. However, the average bond lengths in the semifunctionalized boat conformation range from 1.47 to 1.53 Å, and they remain larger than that in pure graphene. Such increases in the C−C bond length are responsible for the increase in the lattice constant of graphene upon functionalization. The thicknesses of the corrugation (*h*) of the fully functionalized graphenes (chair: h = 0.46−0.54 Å, boat: h = 0.59−0.65 Å) are larger than those of the semifunctionalized graphenes (chair: h = 0.30−0.35 Å, boat: h = 0.40−0.43 Å) because the functionalization of the opposite C atom layer would further pull these C atoms outward so as to meet the geometrical requirement of sp^3 hybridization. *h* of the boat conformation of each functionalized graphene is larger than that of its chair counterpart because the X−C bond (X = F, O, or H) in the boat configuration is slightly slanted with respect to that in the chair configuration, and this slant increases the distance between the two layer C atoms.

To estimate the relative stability of different functionalized graphenes, we define a molar (per atom) Gibbs free energy of formation δG for the functionalized graphenes as:

$$\delta G = E_C + x_C\mu_C + \sum_i x_i\mu_i \quad (1)$$

where $-E_C$ is the cohesive energy per atom of the functionalized graphene, x_C and x_i (i = H, O, or F) are the

TABLE 2. Formation Energies per Atom (δG_{Chair} and δG_{Boat} for the Chair Conformation and Boat Conformation, Respectively) of the Functionalized Graphenes, Graphane, and Graphone

structure	F-graphene	OH-graphene	graphone	O-graphene	F-graphene-H	O-graphene-H	graphane
δG_{Chair} (eV)	0.103	−0.036	0.544	−0.004	−0.439	−0.071	−0.098
δG_{Boat} (eV)	−0.085	−0.211	0.250	0.046	−0.367	−0.041	−0.046

molar fraction of the C atoms and other atoms in the attached groups, respectively, and μ_C and μ_i are the chemical potentials of the constituents at a given state.[30,31] We choose μ_C as the cohesive energy per atom of pristine graphene, μ_H as the 1/2 cohesive energy of the H_2 molecule, μ_O as the 1/2 cohesive energy of the O_2 molecule, and μ_F as the 1/2 cohesive energy of the F_2 molecule. The formation energy as defined above can be regarded as a measure of the stability against molecular desorption from the graphene surface. The stability of differently functionalized graphene is manifested by formation energies; that is, those with more negative formation energies are more stable.

Table 2 presents molar Gibbs free energy of formation (δG) of all the examined functionalized graphenes and those of graphane and graphone for comparison. The chair conformations of the fully functionalized graphenes are slightly more stable than the boat ones by 0.03−0.07 eV per atom, in agreement with previous first-principles density functional predictions.[32] Therefore, both synthesized fully functionalized graphane[18,19] and graphene fluoride[22] should be in the chair conformation if the reaction is thermodynamically controlled. The higher stability of the chair conformations of the fully functionalized graphenes could be attributed to the higher symmetry of their structures. In the chairlike fully functionalized O-graphene-H, F-graphene-H, and graphane, three angles between one X−C (X = F, O, or H) bond and its three nearest C−C bonds are identical, while in the boatlike ones, the angle between the X−C bond and C−C bond II differs from the one between the X−C bond and C−C bond I/III. In the chairlike fully functionalized O-graphene, there are two different angles between the O−C bond and C−C bonds (the angles between the O−C bond and C−C bond I/II are 105.7°/58.2°), while in the boatlike one, there are three different angles between the O−C bond and C−C bonds (the angles between the O−C bond and C−C bond I/II/III are 105.5°/105.6°/57.8°). Therefore, the chair configurations of the fully functionalized graphenes have higher symmetry compared with the boat counterparts, and the C atoms more approach an ideal sp^3 hybridization state. Consequently, the chair configurations of the fully functionalized graphenes have higher stability than the boat ones. The relative stability of the fully functionalized graphenes in the chair configuration decreases in this order: F-graphene-H > graphane > O-graphene-H > O-graphene. In the following work, the less stable boatlike fully functionalized graphenes will not be considered. Unlike the fully functionalized case, the boat configurations are stabilized by 0.18−0.29 eV per atom over the chair ones in the semifunctionalized case. This is due to the formation of C═C double bonds between the two nearest unfunctionalized C atoms in the boat configuration. Similar phenomena also occur in the hydrogenated bilayer graphene described in the previous work.[32] The relative stability of the semifunctionalized graphenes in the boat configuration decreases in this order: OH-graphene > F-graphene > graphone. The actual conformation of semifunctionalized graphenes depends on the reaction path. If we solely functionalize one side of the graphene with the other side intact, we will get the more stable boat conformation. If we first get two-side functionalized graphenes and then remove the functional groups on one side, we are highly likely to get the chair conformation because it is difficult to reconstruct from the chair to the boat configuration due to the totally different group alignments of the two configurations. The formerly predicted ferromagnetic graphone adopted the chair conformation.[26]

Next, we studied the magnetism of the functionalized graphenes. All the checked fully functionalized graphenes are saturated without dangling bonds except the chairlike O-graphene-H, where the O atoms are not saturated. The saturation of the boatlike fully functionalized O-graphene-H is attributed to the fact that the two nearest O atoms form a bond. The boatlike semifunctionalized graphenes are also saturated since C═C double bonds (type III bond in Figure 2b) are formed between the two unfunctionalized C atoms. Therefore, all the boatlike functionalized graphenes and the chairlike O-graphene and F-graphene-H have no magnetism due to their saturated structures. The 2p electrons in the chairlike OH-graphene, F-graphene, and O-graphene-H associated with the unfunctionalized C atoms or the unsaturated O atoms are unpaired, and the extended p−p interactions could induce magnetic coupling between the 2p magnetic moments.[26] Ferromagnetically (FM) coupled (Figure 3a), antiferromagnetically (AFM) coupled (Figure 3b), and nonmagnetic (NM) states are considered for the chairlike OH-graphene, F-graphene, and O-graphene-H, and we have found that the magnetic state is indeed more stable than the nonmagnetic one. The induced magnetic moments of the chairlike F-graphene and OH-graphene are mainly localized on the unfunctionalized C atoms with a value of 0.80 and 0.88 μ_B, respectively

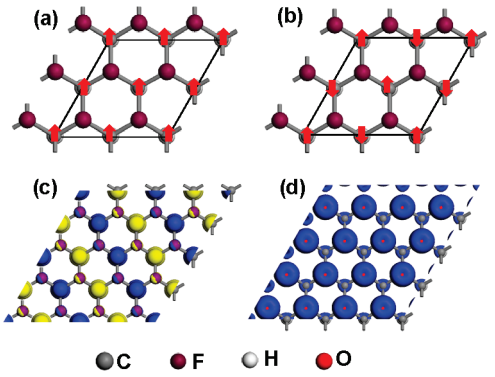

Figure 3. (a) Ferromagnetic and (b) antiferromagnetic configurations of the chairlike functionalized graphenes. Arrows show the relative direction of magnetic moments, and the rhombus marked in black shows the supercell. Spin density of (c) the AFM chairlike F-graphene (isovalue: 0.1 au) and (d) the FM chairlike O-graphene-H (isovalue: 0.08 au). Blue and yellow are used to indicate the positive and negative signs of the spin, respectively.

TABLE 3. Relative Energies Per Supercell of Different Magnetic Configuration States (ferromagnetic: E_{FM}, antiferromagnetic: E_{AFM}, and nonmagnetic: E_{NM}) for the Chairlike Functionalized Graphenes[a]

	chairlike structure		
	F-graphene	OH-graphene	O-graphene-H
E_{FM} (eV)	0.26	0.01	0
E_{AFM} (eV)	0	0	0.18
E_{NM} (eV)	0.52	1.01	0.17
2D T_C *or* T_N (K)	754	29	522
3D T_C *or* T_N (K)	502	19	348

[a] Curie temperature (T_C) and Neel temperature (T_N) are estimated from the energies when these structures are respectively treated as 2D and 3D.

(Figure 3c shows the spin density of the AFM chairlike F-graphene), while the magnetic moments in the chairlike O-graphene-H are chiefly localized on the O atoms (M_O = 0.74 μ_B) and secondarily on the hydrogenated C atoms (M_C = 0.14 μ_B) (Figure 3d). The relative energies of different magnetic configurations of the chairlike F-graphene, OH-graphene, and O-graphene-H are given in Table 3. Both the chairlike F-graphene and the chairlike OH-graphene have AFM ground states, while the chairlike O-graphene-H has a FM ground state.

Using mean-field theory and the energy difference (ΔE) between FM and AFM states of chairlike functionalized graphenes (Table 3), we can estimate Curie temperature (T_C) and Neel temperature (T_N) by the formula $\gamma k_B T_C/2 = E_{AFM} - E_{FM}$ and $\gamma k_B T_N/2 = E_{FM} - E_{AFM}$, in which γ is the dimension, k_B is Boltzmann constant, and E_{AFM} and E_{FM} are energies per cell that contains two C atoms.[26,33,34] Although the mean-field theory often overestimates T_C, it is a useful tool for trend analysis. The previous work suggests that graphone has a Curie temperature of T_C = 278 and 417 K, respectively, when graphone is respectively treated as 3D and 2D. Our calculations show that the Neel temperature of the chairlike F-graphene (T_N(2D) = 754 K and T_N(3D) = 502 K) and the Curie temperature of the chairlike O-graphene-H (T_C(2D) = 522 K and T_C(3D) = 348 K) are higher than T_C of graphone. But the Neel temperature of the chairlike OH-graphene (T_N(2D) = 29 K and T_N(3D) = 19 K) is much lower than T_C of graphone.

The NM boatlike OH-graphene, F-graphene, chairlike O-graphene, and F-graphene-H are all semiconductors as a result of their saturated structures. The NM boatlike OH-graphene and F-graphene have an indirect bandgap of 1.63 and 2.18 eV, respectively (see Figure S1), while the NM chairlike O-graphene and F-graphene-H have a direct bandgap of 3.52 and 3.18 eV, respectively (see Figure S2). The AFM (ground state) chairlike OH-graphene is also a semiconductor with a direct bandgap of 0.60 eV (see Figure S2). The band structure of the FM chairlike OH-graphene is displayed in Figure 4a. It is highly spin polarized, and the bandgap is 0.40 and 4.58 eV in the minority and majority spin channels, respectively. The band structure of the FM chairlike O-graphene-H is shown in Figure 4b. Both spin channels are metallic. There is a large exchange splitting of the conduction bands across the Fermi level (E_f), and the conduction band maxima are 0.47 and 1.44 eV above E_f for the majority and minority spins, respectively. Thus only minority spin has nonvanishing transmission probability in the 0.47−1.44 eV energy range above E_f, whereas the majority spin transmission is prohibited. Consequently, the minority spin current is expected to be much larger than the majority one under a large bias, suggestive of potential applications of the O-graphene-H in spin-filters. Figure 4c and d show the band structures of the AFM and FM chairlike F-graphene, respectively. The AFM (ground state) chairlike F-graphene is a semiconductor with an indirect bandgap of 1.17 eV, and the FM state has a metallic nature. The conductivity of the chairlike F-graphene can be significantly changed if a magnetic field is applied and stabilizes the FM state. This suggests that a spin-valve with GMR could be built out of the chairlike F-graphene.

The two-probe models of the chairlike O-graphene-H and F-graphene-based devices are depicted in Figure 5a and b, respectively. The FM chairlike O-graphene-H itself is used as metallic electrodes; thus the scattering region is identical to the electrodes (Figure 5a). We chose the semiplanar nonmagnetic graphene as electrodes to connect a chairlike F-graphene sheet, which is 2.6 nm wide along the transport direction, and an arch deformation occurs in the scattering region upon optimization (Figure 5b).

The spin-polarized zero-bias transmission spectra $T(E)$ of the chairlike O-graphene-H is presented in Figure 6a. The transmission coefficients at E_f in the minority spin channel are apparently larger than those

in the majority spin channel. We define the spin-filter efficiency (SFE) at zero bias as

$$\mathrm{SFE} = \frac{T_{\mathrm{min}}(E_f) - T_{\mathrm{maj}}(E_f)}{T_{\mathrm{min}}(E_f) + T_{\mathrm{maj}}(E_f)} \quad (2)$$

where $T_{\mathrm{min}}(E_f)$ and $T_{\mathrm{maj}}(E_f)$ represent the transmission coefficient of the minority and majority spin channels at E_f, respectively. The calculated SFE at zero bias is 35%. The spin-polarized $I-V_{\mathrm{bias}}$ curves of the chairlike O-graphene-H model are shown in Figure 6b, where I is the current density for the two-dimensional device. Obviously the total current density remains dominated by the minority spin. We define the spin-filter efficiency at the finite bias voltage as

$$\mathrm{SFE} = \frac{I_{\mathrm{min}} - I_{\mathrm{maj}}}{I_{\mathrm{min}} + I_{\mathrm{maj}}} \quad (3)$$

where I_{min} and I_{maj} represent minority and majority spin current density, respectively. We present the SFE *versus* V_{bias} curve in Figure 6c. With the increase of the bias voltage, the current density of the minority spin increases significantly, but that of the majority spin saturates at about V_{bias} = 0.4 V after a slight increase (Figure 6b). As a result, the SFE increases with the increasing bias and reaches 54% at V_{bias} = 0.6 V (Figure 6c). Therefore, the ferromagnetic metallic chairlike O-graphene-H can produce spin-polarized current.

To understand bias dependence of SFE of the homogeneous chairlike O-graphene-H-based device, we study the bias-dependent electronic structure of the chairlike O-graphene-H electrode and the transmission spectra of the device (Figure 7). At zero bias, the transmission of this homogeneous device is perfect, and the transmission probability is determined only by the number of states whose momentums have a component toward the transport direction. Roughly the SFE at zero bias can be estimated from the following expression:

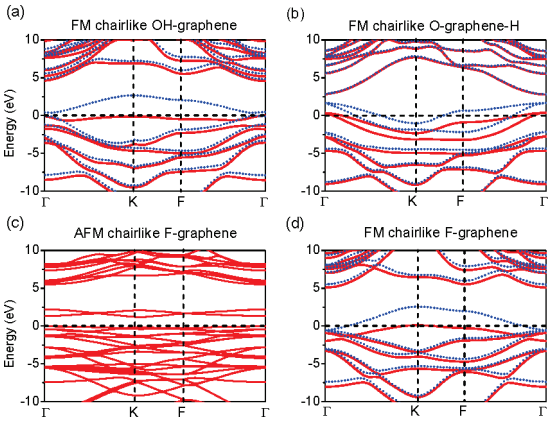

Figure 4. Band structures of the chairlike (a) FM OH-graphene, (b) FM O-graphene-H, (c) AFM F-graphene, and (d) FM F-graphene. Red solid (blue dashed) line represents the majority (minority) spin channel. In panel (c), the two spins are degenerate. The Fermi level is set to zero.

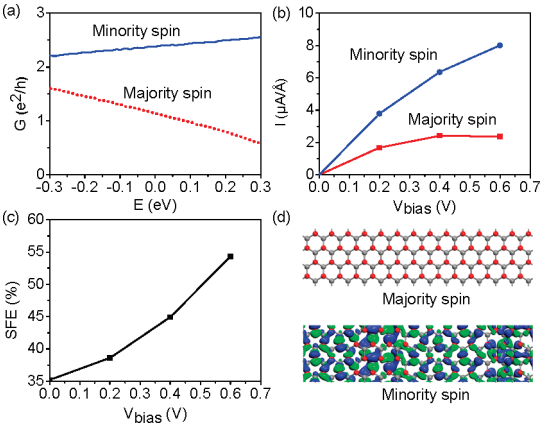

Figure 6. (a) Spin-polarized zero-bias transmission spectra. The Fermi level is set to zero. (b) Spin-resolved $I-V_{\mathrm{bias}}$ curve. (c) Bias dependence of the SFE (spin-filter efficiency) of the chairlike O-graphene-H-based spin-filter device. (d) Isosurfaces of the spin-resolved eigenchannels with the chief transmission probability of the Γ point at E = 0.2 V under V_{bias} = 0.6 V (isovalue: 0.03 au).

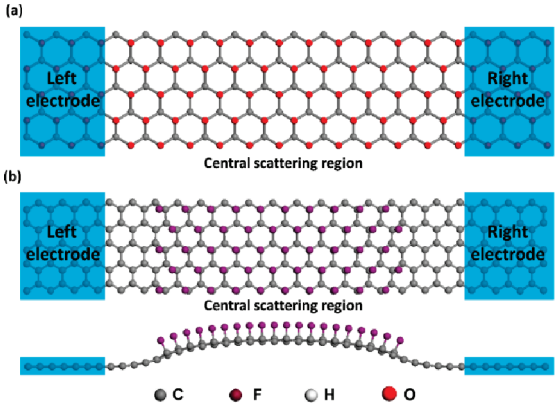

Figure 5. (a) Schematic of a relaxed two-probe model of a chairlike O-graphene-H-based spin-filter device. The FM chairlike O-graphene-H itself is used as metallic electrodes. (b) Top and side views of a schematic model of a chairlike F-graphene-based spin-valve device. The chairlike F-graphene sheet, which is 2.6 nm wide along the transport direction, is connected to semiplanar nonmagnetic graphene electrodes.

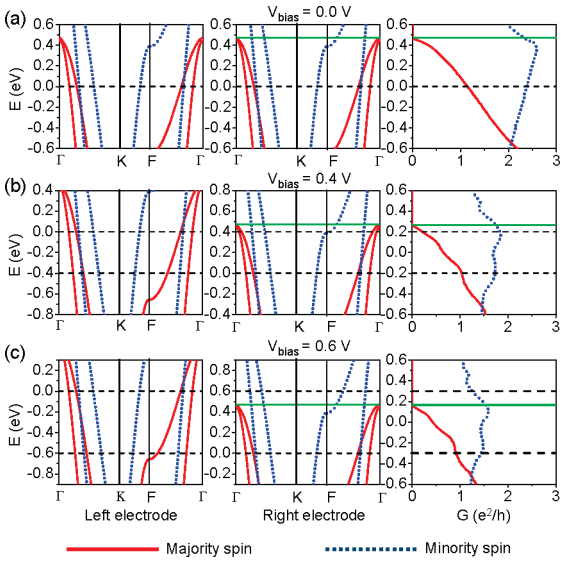

Figure 7. Band structures of the left (left panel) and right (middle panel) electrodes and the spin-resolved transmission spectra (right panel) of the chairlike O-graphene-H device at a bias of (a) 0 V, (b) 0.4 V, and (c) 0.6 eV. Red line (blue dots) represents the majority (minority) spin channel. The dashed black line represents the bias window. The solid green lines in the middle and right panels represent the valence maximum of the right electrode and the top of the nontrivial transmission spectra of the majority spin, respectively. The Fermi level is set to zero.

$$\mathrm{SFE} = \frac{N(E_f)_{\min} - N(E_f)_{\mathrm{maj}}}{N(E_f)_{\min} + N(E_f)_{\mathrm{maj}}} \quad (4)$$

where $N(E_f)_{\min}$ and $N(E_f)_{\mathrm{maj}}$ are the densities of states (DOS) of the minority and majority spins at E_f, respectively. The calculated spin-resolved DOS is given in Figure S3 of Supporting Information, and the estimated SFE is 21%, which is slightly smaller than the exact one (35%). At zero bias, the transmission coefficient of the minority spin first slightly increases with E and then decreases at E = 0.37 eV, and that of the majority spin decreases rapidly with E and vanishes at E = 0.47 eV due to the opening of the bandgap from this energy. At finite bias V_{bias}, E_f of the right and left electrode are shifted by $V_{\mathrm{bias}}/2$ and $-V_{\mathrm{bias}}/2$, respectively. The transmission spectrum of the minority spin is slightly depressed by V_{bias}. As a result, the current density of the minority spin increases with V_{bias} but is smaller than a linear way. The top of the nontrivial transmission spectrum of the majority spin drops with the increasing V_{bias} as a result of the drop of the valence maximum of the right electrode (Figure 7b and c). Consequently, a zero transmission region appears in the bias window (Figure 7c), and its range linearly increases with V_{bias}. At V_{bias} = 0.6 V, this range is 0.13 eV (Figure 7c). As a result, the current density of the majority spin changes slightly with V_{bias} because the integral area of the transmission spectrum of the majority spin within the bias window is changed slightly. SFE is a ratio of the two current densities and thus increases with V_{bias}. Higher SFE over 54% is also expected under a larger bias as a result of the mechanism discussed above. We also show the spin-resolved eigenchannels with the chief transmission probability of the Γ point at E = 0.2 V under V_{bias} = 0.6 V (Figure 6d).

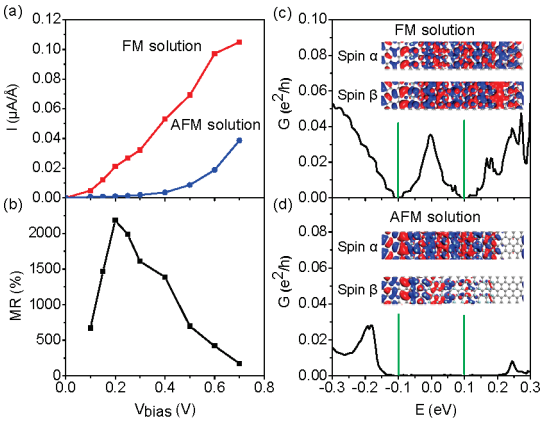

Figure 8. (a) $I-V_{\mathrm{bias}}$ curve, (b) bias dependence of the magnetoresistances, and 0.2 V bias transmission spectra of the (c) FM and (d) AFM solutions of the chairlike F-graphene-based spin-valve device. The green lines represent the bias window. Insets: isosurfaces of the spin-resolved eigenchannels with the chief transmission probability of the Γ point at E_f under V_{bias} = 0.2 V of the corresponding solutions (isovalue: 0.05 au). The Fermi level is set to zero.

There are no eigenchannels of the majority spin, while the eigenchannel of the minority spin (with an eigenvalue of 0.978) extends over the device.

The total current densities of the FM and AFM solutions *versus* V_{bias} curves of the chairlike F-graphene model are shown in Figure 8a. As we expect, the total current density in the FM solution is significantly greater than that in the AFM solution. Figure 8c and d present the 0.2 V bias transmission spectra of the FM and AFM solutions, respectively. The transmission coefficients within the bias window of the FM solution are much larger than those of the AFM solution. This great difference of conductance between the two

solutions is due to the different conducting mechanism (metallic *versus* tunneling). The spin-resolved eigenchannels with the chief transmission probability of the Γ point at E_f under V_{bias} = 0.2 V are shown in the insets of Figure 8c and d for the FM and AFM solutions, respectively. The eigenchannels of the FM solution (with eigenvalues of 0.787 and 0.835 for α and β spins, respectively) extend over the device, while those of the AFM solution (with eigenvalues of 0.012 and 0.002 for α and β spins, respectively) decay quickly and cannot reach the right electrode, confirming much larger conductance of the FM solution than that of the AFM solution. Magnetoresistance is defined as

$$\mathrm{MR} = \frac{I_{FM} - I_{AFM}}{I_{AFM}} \quad (5)$$

where I_{FM} and I_{AFM} represent current density of the FM and AFM solution, respectively. We present the room-temperature MR *versus* V_{bias} curve in Figure 8b. The MR first increases with the increasing bias and peaks at 2200% when V_{bias} = 0.2 V and then starts to decay. The maximum experimental room-temperature MR values are a few hundred percent,[35−37] and the theoretical maximum room-temperature MR of our spin-valve is thus 1 order of magnitude larger than the available experimental maximum values and 2 orders of magnitude larger than the maximum room-temperature MR obtained on the spin-valve built from pure graphene.[7] The highest room-temperature MR obtained in the experiments[35−37] is tunnel magnetoresistance (TMR). In this type of spin-valve, the relative spin polarization direction of the two ferromagnets on the two electrodes is tuned by the external magnetic field. When the spin polarization direction of the two electrodes is parallel (P), the electrons are always allowed to pass the device in a tunneling way because their spin states are matched on the two electrodes. When the spin polarization direction of the two ferromagnets is antiparallel (AP), the electrons with mismatching spin state on the two electrodes are forbidden to pass the device, and thus the resistance in the AP orientation is larger than that in the parallel orientation. However, in the experimental ferromagnets,[35−37] the spin states in the AP configuration on the two electrodes are not completely mismatched, and there still are electrons tunneling through the device due to the small amount of spin matching on the two electrodes. The mechanism of the spin-valve proposed by us is quite different. We make use of the substantial conduction difference between the semiconducting AFM ground state and metallic FM excited state. The transmission of electrons in the AFM solution is in principle fully forbidden when the channel of the device is long enough. Thus higher MR is obtained in our spin-valve than the experiments based on TMR.[35−37]

Our theoretical maximum room-temperature MR for the chairlike F-graphene spin-valve is much lower than the theoretical values of 10^6−10^9 for the first type ZNGR spin-valves[9,10] but comparable with that of the second type ZGNR spin-valve (unpublished data) since our chairlike F-graphene spin-valve has an identical working mechanism with that of the second type ZGNR spin-valve. When the bias voltage increases to 0.5 eV, the current density in the AFM solution increases significantly and the MR decreases to 700%. The depressed MR with the increasing bias is also found in ZGNR spin-valves.[9,10]

CONCLUSION

By first-principles calculations, we demonstrate that functionalization of a nonmagnetic graphene can lead to stable novel magnetic materials with high spin-filter efficiency and giant room-temperature magnetoresistance comparable with that of graphene nanoribbons. This renders functionalized graphene a promising material for high-performance two-dimensional spintronics devices. Compared with ultranarrow graphene nanoribbon spintronics devices, functionalized graphenes allow much larger current with lower requirement in fabrication technique and are more competitive.

METHODS

The geometry optimization and electronic properties are calculated by using the ultrasoft pseudopotentials plane-wave method, as implemented in the CASTEP code.[38,39] The generalized gradient approximation (GGA) of the Perdew−Burke−Ernzerhof (PBE)[40] form is employed for the exchange−correlation functional. The reciprocal space was represented by a Monkhorst−Pack[41] special *k*-point scheme with 12×12×1 grid meshes. We have constructed supercells consisting of eight carbon atoms to check the magnetism of our functionalized graphenes. All supercells are large enough to ensure that the vacuum space is at least 10 Å, so that the interaction between functionalized graphenes and their periodic images can be safely avoided. Both the atomic positions and lattices are relaxed without any symmetry constraints with a plane-wave cutoff energy of 400 eV. The convergence criteria of energy and force are set to 1×10^{-5} eV and 0.03 eV/Å, respectively. The accuracy of our procedure is tested by calculating the C−C bond length of graphene: our calculated result of 1.42 Å is the same as the experimental value.

A two-probe model is constructed to study the transport properties. The transport properties are computed by using the DFT coupled with the NEGF formalism implemented in the ATK code.[42−44] The local density approximation (LDA) and norm-conserving pseudopotentials of the Troullier−Martins type[45] are used. The single-zeta polarized basis set (SZP) is used, and the mesh cutoff is chosen as 150 Ry. The electron temperature is set to 300 K. The structures of the scattering region are optimized until the maximum atomic force is less than 0.03 eV/Å. The spin-resolved current I_σ under bias voltage V_{bias} is calculated with the Landauer−Büttiker formula:[46]

$$I_\sigma(V_{bias}) = \frac{e}{h}\int \{T_\sigma(E, V_{bias})[f_L(E, V_{bias}) - f_R(E, V_{bias})]\}\mathrm{d}E \quad (6)$$

where $T_\sigma(E,V_{bias})$ is the spin-resolved transmission probability,

$f_{L/R}(E,V_{bias})$ is the Fermi–Dirac distribution function for the left (L)/right (R) electrode, and σ is a spin index. The noncollinear spin orientation effect is neglected due to the absence of domain wall in our calculations.

Acknowledgment. This work was supported by the NSFC (Grant Nos. 10774003, 90626223, and 20731162012), National 973 Projects (No. 2007CB936200, MOST of China), Program for New Century Excellent Talents in University of MOE of China, Fundamental Research Funds for the Central Universities, and National Foundation for Fostering Talents of Basic Science (No. J0630311).

Supporting Information Available: Band structures of the NM boatlike OH-graphene, NM boatlike F-graphene, NM chairlike O-graphene, NM chairlike F-graphene-H, and AFM chairlike F-graphene; density of states of the FM O-graphene-H. This material is available free of charge *via* the Internet at http://pubs.acs.org.

REFERENCES AND NOTES

1. Berger, C.; Song, Z. M.; Li, T. B.; Li, X. B.; Ogbazghi, A. Y.; Feng, R.; Dai, Z. T.; Marchenkov, A. N.; Conrad, E. H.; First, P. N.; *et al.* Ultrathin Epitaxial Graphite: 2D Electron Gas Properties and a Route toward Graphene-Based Nanoelectronics. *J. Phys. Chem. B* **2004,** *108*, 19912–19916.
2. Novoselov, K. S.; Geim, A. K.; Morozov, S. V.; Jiang, D.; Zhang, Y.; Dubonos, S. V.; Grigorieva, I. V.; Firsov, A. A. Electric Field Effect in Atomically Thin Carbon Films. *Science* **2004,** *306*, 666–669.
3. Novoselov, K. S.; Geim, A. K.; Morozov, S. V.; Jiang, D.; Katsnelson, M. I.; Grigorieva, I. V.; Dubonos, S. V.; Firsov, A. A. Two-Dimensional Gas of Massless Dirac Fermions in Graphene. *Nature* **2005,** *438*, 197–200.
4. Berger, C.; Song, Z. M.; Li, X. B.; Wu, X. S.; Brown, N.; Naud, C.; Mayou, D.; Li, T. B.; Hass, J.; Marchenkov, A. N.; *et al.* Electronic Confinement and Coherence in Patterned Epitaxial Graphene. *Science* **2006,** *312*, 1191–1196.
5. Geim, A. K.; Novoselov, K. S. The Rise of Graphene. *Nat. Mater.* **2007,** *6*, 183–191.
6. Novoselov, K. S.; Morozov, S. V.; Mohinddin, T. M. G.; Ponomarenko, L. A.; Elias, D. C.; Yang, R.; Barbolina, I. I.; Blake, P.; Booth, T. J.; Jiang, D.; *et al.* Electronic Properties of Graphene. *Phys. Status Solidi B* **2007,** *244*, 4106.
7. Hill, E. W.; Geim, A.; Novoselov, K.; Schedin, F.; Blake, P. Graphene Spin Valve Devices. *IEEE Trans. Magn.* **2006,** *42*, 2694.
8. Wang, W. H.; Pi, K.; Li, Y.; Chiang, Y.; Wei, P.; Shi, J.; Kawakami, R. Magnetotransport Properties of Mesoscopic Graphite Spin Valves. *Phys. Rev. B* **2008,** *77*, 020402(R).
9. Kim, W. Y.; Kim, K. S. Prediction of Very Large Values of Magnetoresistance in a Graphene Nanoribbon Device. *Nat. Nanotechnol.* **2008,** *3*, 408–412.
10. Qin, R.; Lu, J.; Lai, L.; Zhou, J.; Li, H.; Liu, Q. H.; Luo, G. F.; Zhao, L. N.; Gao, Z. X.; Mei, W. N.; *et al.* Room-Temperature Giant Magnetoresistance over One Billion Percent in a Bare Graphene Nanoribbon Device. *Phys. Rev. B* **2010,** *81*, 233403.
11. Muñoz-Rojas, F.; Fernández-Rossier, J.; Palacios, J. J. Giant Magnetoresistance in Ultrasmall Graphene Based Devices. *Phys. Rev. Lett.* **2009,** *102*, 136810.
12. Son, Y. W.; Cohen, M. L.; Louie, S. G. Half-Metallic Graphene Nanoribbons. *Nature* **2006,** *444*, 347–349.
13. Kan, E. J.; Li, Z. Y.; Yang, J. L.; Hou, J. G. Half-Metallicity in Edge-Modified Zigzag Graphene Nanoribbons. *J. Am. Chem. Soc.* **2008,** *130*, 4224–4228.
14. Lai, L.; Lu, J.; Wang, L.; Luo, G. L.; Zhou, J.; Qin, R.; Chen, Y.; Li, H.; Gao, Z. X.; Li, G. P.; *et al.* Magnetism in Carbon Nanoscrolls: Quasi-Half-Metal and Half-Metal in Pristine Hydrocarbon. *Nano Res.* **2009,** *2*, 844–850.
15. Lu, W.; Lieber, C. M. Nanoelectronics from the Bottom Up. *Nat. Mater.* **2007,** *6*, 841–850.
16. Duan, X. F. Assembled Semiconductor Nanowire Thin Films for High-Performance Flexible Macroelectronics. *MRS Bull.* **2007,** *32*, 134–141.
17. Sofo, J. O.; Chaudhari, A. S.; Barber, G. D. Graphane: A Two-Dimensional Hydrocarbon. *Phys. Rev. B* **2007,** *75*, 153401.
18. Elias, D. C.; Nair, R. R.; Mohiuddin, T. M. G.; Morozov, S. V.; Blake, P.; Halsall, M. P.; Ferrari, A. C.; Boukhvalov, D. W.; Katsnelson, M. I.; Geim, A. K.; *et al.* Control of Graphene's Properties by Reversible Hydrogenation: Evidence for Graphane. *Science* **2009,** *323*, 610–613.
19. Liu, L.; Ryu, S. M.; Tomasik, M. R.; Stolyarova, E.; Jung, N.; Hybertsen, M. S.; Steigerwald, M. L.; Brus, L. E.; Flynn, G. W. Graphene Oxidation: Thickness-Dependent Etching and Strong Chemical Doping. *Nano Lett.* **2008,** *8*, 1965–1970.
20. Li, Y. F.; Zhou, Z.; Shen, P. W.; Chen, Z. F. Structural and Electronic Properties of Graphane Nanoribbons. *J. Phys. Chem. C* **2009,** *113*, 15043–15045.
21. Eda, G.; Chhowalla, M. Chemically Derived Graphene Oxide: Towards Large-Area Thin-Film Electronics and Optoelectronics. *Adv. Mater.* **2010,** *22*, 2392–2415.
22. Cheng, S. H.; Zou, K.; Okino, F.; Gutierrez, H. R.; Gupta, A.; Shen, N.; Eklund, P. C.; Sofo, J. O.; Zhu, J. Reversible Fluorination of Graphene: Evidence of a Two-Dimensional Wide Bandgap Semiconductor. *Phys. Rev. B* **2010,** *81*, 205435.
23. Robinson, J. T.; Burgess, J. S.; Junkermeier, C. E.; Badescu, S. C.; Reinecke, T. L.; Perkins, F. K.; Zalalutdniov, M. K.; Baldwin, J. W.; Culbertson, J. C.; Sheehan, P. E.; *et al.* Properties of Fluorinated Graphene Films. *Nano Lett.* **2010,** *10*, 3001–3005.
24. Nair, R. R.; Jalil, R.; Riaz, I.; Kravets, V. G.; Britnell, L.; Blake, P.; Schedin, F.; Mayorov, A. S.; Yuan, S.; Katsnelson, M. I.; *et al.* Fluorographene: Two Dimensional Counterpart of Teflon. arXiv:1006.3016, *Small* (to be published).
25. Charlier, J. C.; Gonze, X.; Michenaud, J. P. First-Principles Study of Graphite Monofluoride $(CF)_n$. *Phys. Rev. B* **1993,** *47*, 16162–16168.
26. Zhou, J.; Wang, Q.; Sun, Q.; Chen, X. S.; Kawazoe, Y.; Jena, P. Ferromagnetism in Semihydrogenated Graphene Sheet. *Nano Lett.* **2009,** *9*, 3867–3870.
27. Holtzl, T.; Veszpremi, T.; Minh, T. N. Phosphaethyne Polymers Are Analogues of Cis-Polyacetylene and Graphane. *Cr. Chim.* **2010,** *13*, 1173–1179.
28. Bieri, M.; Treier, M.; Cai, J. M.; Ait-Mansour, K.; Ruffieux, P.; Groning, O.; Groning, P.; Kastler, M.; Rieger, R.; Feng, X. L.; *et al.* Porous Graphenes: Two-Dimensional Polymer Synthesis with Atomic Precision. *Chem. Commun.* **2009,** 6919–6921.
29. Lee, E. C.; Choi, Y. C.; Kim, W. Y.; Singh, N. J.; Lee, S.; Shim, J. H.; Kim, K. S. A Radical Polymer as a Two-Dimensional Organic Half Metal. *Chem.—Eur. J.* **2010,** *16*, 12141–12146.
30. Barone, V.; Hod, O.; Scuseria, G. E. Electronic Structure and Stability of Semiconducting Graphene Nanoribbons. *Nano Lett.* **2006,** *6*, 2748–2754.
31. Li, L. Z.; Li, H.; Zhou, J.; Lu, J.; Qin, R.; Gao, Z. X.; Mei, W. N. Electronic Structure and Stability of Ultranarrow Single-Layer SnS_2 Nanoribbons: a First-Principles Study. *J. Comput. Theor. Nanos* **2010,** *7*, 2100–2103.
32. Samarakoon, D. K.; Wang, X. Q. Tunable Band Gap in Hydrogenated Bilayer Graphene. *ACS Nano* **2010,** *4*, 4126–4130.
33. Zhou, J.; Wang, Q.; Sun, Q.; Jena, P. Electronic and Magnetic Properties of a BN Sheet Decorated with Hydrogen and Fluorine. *Phys. Rev. B* **2010,** *81*, 085442.
34. Kudrnovsky, J.; Turek, I.; Drchal, V.; Maca, F.; Masek, J.; Weinberger, P.; Bruno, P. Ab initio Study of Curie Temperatures of Diluted Magnetic Semiconductors. *J. Supercond.* **2003,** *16*, 119–122.
35. Parkin, S. S. P.; Kaiser, C.; Panchula, A.; Rice, P.; Hughes, B.; Samant, M.; Yang, S. Giant Tunnelling Magnetoresistance at Room Temperature with MgO (100) Tunnel Barriers. *Nat. Mater.* **2004,** *3*, 862–867.
36. Yuasa, S.; Nagahama, T.; Fukushima, A.; Suzuki, Y.; Ando, K. Giant Room-Temperature Magnetoresistance in Single-Crystal Fe/MgO/Fe Magnetic Tunnel Junctions. *Nat. Mater.* **2004,** *3*, 868–871.
37. Ikeda, S.; Hayakawa, J.; Ashizawa, Y.; Lee, Y. M.; Miura, K.; Hasegawa, H.; Tsunoda, M.; Matsukura, F.; Ohno, H. Tunnel

Magnetoresistance of 604% at 300 K by Suppression of Ta Diffusion in CoFeB/MgO/CoFeB Pseudo-Spin-Valves Annealed at High Temperature. *Appl. Phys. Lett.* **2008,** *93*, 082508.
38. Segall, M. D.; Lindan, P. J. D.; Probert, M. J.; Pickard, C. J.; Hasnip, P. J.; Clark, S. J.; Payne, M. C. First-Principles Simulation: Ideas, Illustrations and the CASTEP Code. *J. Phys.: Condens. Mat.* **2002,** *14*, 2717–2744.
39. Clark, S. J.; Segall, M. D.; Pickard, C. J.; Hasnip, P. J.; Probert, M. J.; Refson, K.; Payne, M. C. First Principles Methods Using CASTEP. *Z. Kristallogr.* **2005,** *220*, 567–570.
40. Perdew, J. P.; Burke, K.; Ernzerhof, M. Generalized Gradient Approximation Made Simple. *Phys. Rev. Lett.* **1996,** *77*, 3865–3868.
41. Monkhorst, H. J.; Pack, J. D. Special Points for Brillouin-Zone Integrations. *Phys. Rev. B* **1976,** *13*, 5188–5192.
42. *Atomistix ToolKit* version 2008.10, QuantumWise A/S (www.quantumwise.com).
43. Taylor, J.; Guo, H.; Wang, J. Ab Initio Modeling of Open Systems: Charge Transfer, Electron Conduction, and Molecular Switching of a C_{60} Device. *Phys. Rev. B* **2001,** *63*, 121104.
44. Brandbyge, M.; Mozos, J. L.; Ordejon, P.; Taylor, J.; Stokbro, K. Density-Functional Method for Nonequilibrium Electron Transport. *Phys. Rev. B* **2002,** *65*, 165401.
45. Troullier, N.; Martins, J. L. Efficient Pseudopotentials for Plane-Wave Calculations. *Phys. Rev. B* **1991,** *43*, 1993–2006.
46. Datta, S., *Electronic Transport in Mesoscopic Systems*; Cambridge University Press: Cambridge, England, 1995.